LA-UR-17-21870 (Accepted Manuscript)

Quantum Yield Heterogeneity among Single Nonblinking Quantum Dots Revealed by Atomic Structure-Quantum Optics Correlation

Orfield, Noah Jeremiah
McBride, James R.
Wang, Feng
Buck, Matthew R.
Keene, Joseph D.
Reid, Kema R.
Htoon, Han
Hollingsworth, Jennifer Ann
Rosenthal, Sandra J.

To be published in: ACS Nano

DOI to publisher's version: 10.1021/acsnano.5b05876

Permalink to record: http://permalink.lanl.gov/object/view?what=info:lanl-repo/lareport/LA-UR-17-21870

Quantum Yield Heterogeneity Among Single Nonblinking Quantum Dots Revealed by Atomic Structure-Quantum Optics Correlation

Noah J. Orfield,[†,‡] James R. McBride,[*,†,‡] Feng Wang,[¶] Matthew R. Buck,[¶,@] Joseph D. Keene,[†,‡,△] Kemar R. Reid,[§,‡] Han Htoon,[*,¶] Jennifer A. Hollingsworth,[*,¶] and Sandra J. Rosenthal[*,†,‡,§,∥,⊥,#]

†*Department of Chemistry, Vanderbilt University, Nashville, Tennessee 37235, United States*

‡*Vanderbilt Institute for Nanoscale Science and Engineering, Vanderbilt University, Nashville, Tennessee 37235, United States*

¶*Materials Physics & Applications Division: Center for Integrated Nanotechnologies, Los Alamos National Laboratory, Los Alamos, New Mexico 87545, United States*

§*Department of Interdisciplinary Materials Science, Vanderbilt University, Nashville, Tennessee 37235, United States*

∥*Department of Physics and Astronomy, Vanderbilt University, Nashville, Tennessee 37235, United States*

⊥*Department of Pharmacology, Chemical and Biomolecular Engineering, Vanderbilt University, Nashville, Tennessee 37235, United States*

#*Materials Science and Technology Division, Oak Ridge National Laboratory, Oak Ridge, Tennessee 37831, United States*

@*Present Address: Department of Chemistry, Colgate University, Hamilton, New York 13346, United States*

△*Present address: Department of Chemistry, Mercer University, Macon, Georgia 31207, United States*

E-mail: james.r.mcbride@vanderbilt.edu; htoon@lanl.gov; jenn@lanl.gov; sandra.j.rosenthal@vanderbilt.edu

Abstract

Physical variations in colloidal nanostructures give rise to heterogeneity in expressed optical behavior. This correlation between nanoscale structure and function demands interrogation of both atomic structure and photophysics at the level of single nanostructures to be fully understood. Herein, by conducting detailed analyses of fine atomic structure, chemical composition, and time-resolved single-photon photoluminescence data for the same individual nanocrystals, we reveal inhomogeneity in the quantum yields of single nonblinking "giant" CdSe/CdS core/shell quantum dots (g-QDs). We find that each g-QD possesses distinctive single exciton and biexciton quantum yields that result mainly from variations in the degree of charging, rather than from volume or structure inhomogeneity. We further establish that there is a very limited non-emissive "dark" fraction (<2%) among the studied g-QDs and present direct evidence that the g-QD core must lack inorganic passivation for the g-QD to be "dark". Therefore, in contrast to conventional QDs, ensemble photoluminescence quantum yield is principally defined by charging processes rather than the existence of dark g-QDs.

In colloidal quantum dot (QD) heterostructures, dissimilarity in physical structure and morphology is intimately tied to electronic structure variations that have a profound influence on the expressed absorption and emission properties.[1] At the same time, commercial prospects for QDs are expanding rapidly, with successful incorporation of QDs into LEDs,[2] displays,[3] lasers,[4] and sensors.[5] Single QDs are also intriguing for use as single photon emitters,[6] entangled photon-pair emitters,[7,8] and biological labelling agents.[9] Despite the pronounced rise in efficiencies and availability of QD-based devices, much about the fundamental physics of QDs is still unknown—specifically, regarding the effects of atomic-scale defects and inhomogeneities on the expression of photoluminescence and absorption.[10,11] This fundamental understanding is crucial at the current stage of colloidal QD development.

Ensemble measurements, while informative, fail to provide insights into the effects of fine structural variance on photophysical properties. Single QD spectroscopy has been incredibly useful in elucidating the nature and mechanism of, for example, single QD photoluminescence

intermittency,[12,13] and studies incorporating correlation of single QD photoluminescence data with structural measurements from atomic force microscopy (AFM)[14] and transmission electron microscopy (TEM)[15,16] have proven informative. However, AFM fails to provide detailed structural information such as lattice defects and shell epitaxy, while TEM have these same drawbacks accompanying a difficult correlation procedure that struggles to produce ambiguous identification of the same QD because of the low contrast of the electron microscopy method.[16] A comprehensive description of the effects of size, shape, and structural inhomogeneities—a feat beyond the reach of conventional AFM and TEM correlation—is imperative in order to understand the underlying physics inherent in QD optical expression.

When a QD is struck by a laser pulse, the probability of a photon being absorbed is directly related to the size of the QD. Further, the fate of an exciton generated within the QD is dictated by the electronic environment, which is highly dependent upon the physical properties of the QD. The core size is the best known physical parameter on which electronic structure depends—the larger the core, the lower the energy of photons that are able to be absorbed and emitted. There are, however, many other physical parameters that directly influence the energy and characteristic time in which the exciton radiatively recombines. For example, structural defects can induce nonradiative recombination, which competes directly with radiative emission as a potential outcome of exciton formation.[10] Therefore, studying exciton outcomes in single QDs as a function of structural and morphological differences provides insight into the charge transport properties and energy conversion efficiency of films and arrays made from colloidally synthesized QDs.

Recently, we achieved correlation of time-resolved photoluminescence data with atomic structure in commercially available core/shell QDs.[10] This correlation allowed an understanding of the delicate effects–on a single QD basis–of defects, crystal structure and shell epitaxy on the photoluminescence behavior of individual QDs. Herein, we extend this approach to "giant" CdSe/CdS core/thick-shell quantum dots (g-QDs)[17–19] to address outstanding issues pertaining to their unique photophysical properties. g-QDs exhibit suppressed blinking

behavior on the single-dot level, and also show significantly reduced Auger recombination rates due to the presence of a thick CdS shell.[20] Intriguingly, although essentially complete suppression of blinking has been recently realized for this system,[18,19] ensemble quantum yields have generally remained well below unity. Previous work has suggested that a non-emissive "dark" fraction may be contributing to sub-optimal quantum yields;[21] however, in that case the non-blinking fraction had also not been optimized, leaving open the challenge to reconcile a fully non-blinking behavior with relatively low QYs (<50%). In this study, we determined the chemical composition of the same individual QD heterostructures for which we had previously acquired extensive photoluminescence data, as shown in Figure 1a.

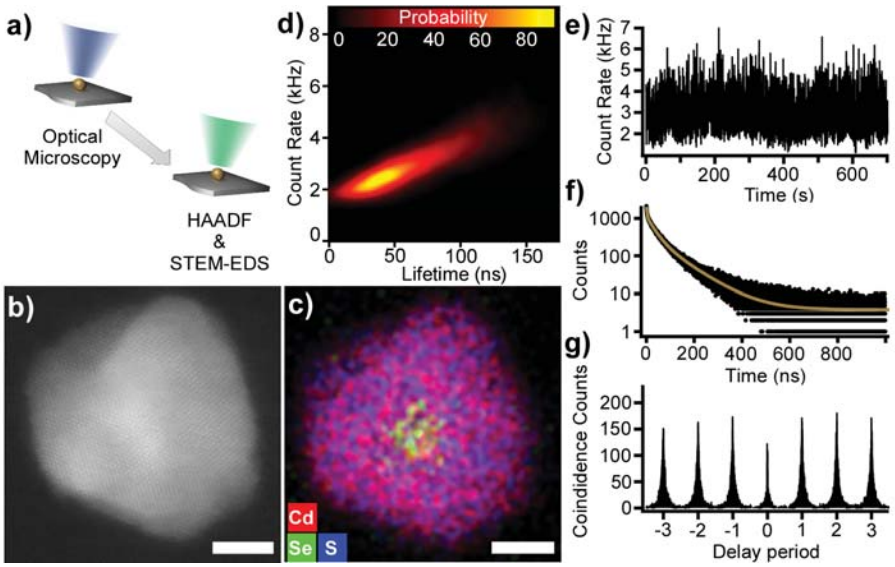

Figure 1: **Acquisition of optical, structural and chemical data for a single colloidal quantum dot.** (a) An individual quantum dot is located on a SiO_2 substrate and sequentially imaged *via* optical spectroscopy and high-resolution electron microscopy according to a previously published method.[10] The measurable parameters from the very same single colloidal quantum dot include (b) fine atomic structure, (c) spatially-resolved chemical composition, (d) fluorescence-lifetime intensity distribution plots (FLIDs), (e) photoluminescence time trace, (f) photoluminescence lifetime, and (g) second-order fluorescence intensity correlation ($g^{(2)}$). The location of the CdSe core can be determined from the EDS mapping trace of selenium in (c). Because the lifetime and intensity of the QD photoluminescence varies over time, both are calculated for each time bin (every 100 ms); plotting the lifetime *vs* intensity for each bin provides a 2D heatmap histogram (d) that facilitates visualization of exciton dynamics over long time scales. Probability in (d) reflects the likelihood of the QD to emit from a specific correlated lifetime-intensity state. Scale bars in (b) and (c) are 5 nm.

In the past, usage of high angle annular dark field (HAADF) detection on a scanning transmission electron microscope (STEM) (Figure 1b) has allowed for identification of core location *via* differential contrast based upon atomic number.[22] However, when studying bulkier structures than traditional core/shell nanocrystals, such as the g-QDs studied here, the large shell volume inhibits the sensitivity of HAADF to determine the location of higher atomic number elements within the heterostructures. Additionally, because HAADF intensity is indicative of both atomic number contrast and sample thickness, implementation of HAADF imaging to locate cores in core/shell QDs is a somewhat qualitative exercise. For this study, we have used STEM paired with energy dispersive X-ray spectroscopy (STEM-EDS, Figure 1c) to provide a much more complete picture of the chemical structure of the QD. This measurement allows visualization of QD–to–QD variations in location of the CdSe core. The minimum observable distance between the core and the surface of the g-QD heterostructure can then be correlated to specific PL behaviors. With our expanded correlation toolset, we are able to probe the relationship between a plethora of parameters, including core location (*via* single-QD STEM-EDS), surface roughness (*via* 2D perimeter), absorption cross-section, PL intensity time trace (Figure 1e), PL radiative decay lifetime (Figure 1f), and second-order fluorescence intensity correlation ratio $g^{(2)}$ (Figure 1g). We can also record the trajectory of both PL lifetime and PL intensity over time. These parameters can then be histogrammed to provide insight into changes in the exciton recombination pathway as a function of time, as demonstrated in the fluorescence lifetime intensity distribution in Figure 1d. The $g^{(2)}$ measurement (Figure 1g) indicates the likelihood of biexciton emission from a single quantum dot after biexciton formation due to a single laser pulse.[7] Any time two photons are sequentially emitted after excitation by one pulse, a count is registered around the zero-time delay peak. Therefore, the area ratio of the center peak to the side peaks of $g^{(2)}$ is typically used as a means to measure biexciton quantum yield relative to that of single exciton quantum yield (BXQY/SXQY). This measurement also provides a good indication of the ability of a QD to emit radiatively under high pump fluence (when biexciton

formation is more likely) and has been shown to be heterogeneous among as-synthesized QD samples—making study of structural dependence vital to QD development.[8,23]

Although g-QDs are non-blinking (100% nonblinking fraction, see Supporting Information), they still exhibit intensity variations in average PL intensity from dot to dot. Without a structural correlation, these emission variations could reasonably be attributed to corresponding variation in the volume of single g-QDs. Because the volume (and absorption cross-section) of g-QDs changes substantially with as little as a single-monolayer of variation, the heterodispersity of g-QDs demands single QD QY measurements in order to understand if variations in emission intensity are due to changes in single QD QY or changes in QD size. Here, we have used intensities acquired from HAADF-STEM to facilitate precise determination of the absorption cross-section for every individual QD on which we performed single QD spectroscopy. This measurement, along with measured photoluminescence (PL) intensity, was used to determine the QY of each g-QD relative to all other QDs.

Results and discussion

For this study, we examined 24 individual g-QDs from the same synthetic batch. Full details on synthesis are available in the Supporting Information. The QY distribution of this sample is shown in Figure 2a—it is apparent from this plot that there was an inherent inhomogeneity in the distribution of single QD QYs.

The average of the QYs that were measured was 43%. It is important to note that the QYs presented here are relative, and the QD assigned a QY value of 1 likely possessed a value somewhat smaller than unity. Therefore, the 43% value is a slight overestimate of the mean QY expressed by single QDs. We also noted a large gap between the three highest QYs and the rest of the measured QYs.

This observed QY heterogeneity became more intriguing when searching for "dark" QDs. Previous studies of traditional QDs have demonstrated that a "dark fraction" of permanently

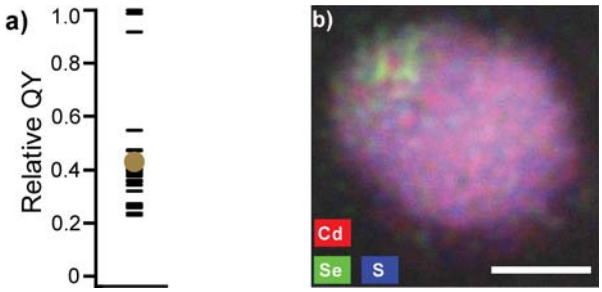

Figure 2: **Quantum yield heterogeneity among single nonblinking QDs.** (a) The g-QDs display a heterogeneous distribution of single-QD quantum yields. The gold point represents the mean of the single-QD measurements. (b) HAADF / EDS overlay of the single nonemissive dot found in the examined sample. This particle was the lone g-QD with an exposed (unpassivated) CdSe core, as demonstrated in the EDS map. On the whole, we find that QY heterogeneity, and not a significant "dark" fraction, accounts for the measured ensemble PLQY. Scale bars are 5 nm.

nonradiative QDs contributes negatively to ensemble QD photoluminescence (PL).[14,24] In the past, we have shown the unique ability to probe the precise atomic structure of "dark" QDs.[10] With this in mind, we set out to determine a unique structural motif among "dark" QDs in the overall g-QD population. To aid in the investigation of the "dark" fraction, a g-QD sample was chosen that exhibits good nonblinking PL behavior on the individual QD level, but an ensemble photoluminescence quantum yield (PLQY) of ∼30%. For the purpose of examining this "dark" fraction, the sample size was expanded to >50 QDs; in total, only 1 g-QD was observed to be permanently nonradiative, and it had an unpassivated CdSe core (Figure 2b). In light of these results, the measured ensemble QY (∼30%) is attributed to variation in the single-QD QY, and not to the presence of a large "dark fraction" of QDs. The lack of a substantial population of "dark" QDs is notable—this observation runs contrary to those made by several groups in the past in work on traditional QDs.[14,24] More broadly, we have determined that in order for a QD to be in the "dark" population, some portion of the CdSe core must be unpassivated by the shell material—an assertion that is supported by previous study.[10,25] This would explain the presence of only one observed "dark" g-QD; the large successive ionic layer adsorption and reaction (SILAR) grown CdS shell provides complete surface passivation of the CdSe core for nearly every studied QD.

Notably, three of the g-QDs had a remarkably high QY when compared to the rest of the sample, as can be seen in Figure 2a. On the other hand, Figure 2a also demonstrates that the QY of the remaining individual g-QD population is much lower, and varies from QD-to-QD. As an explanation for this single-QD QY variation, we attempted to implicate a specific structural factor *via* analysis of QD structure. There is, however, no observed relationship between structural properties and QY (Figure S2). Additionally, visual inspection of individual g-QDs did not reveal specific morphological or structural features that are tied to high single-QD QY (see Supporting In-formation for full structures and PL of all g-QDs).

It is important to note that none of the g-QDs with non-unity average QY has a maximum single-QD QY near-unity. As shown Figure 3a, the average QY (determined from the integrated single-QD photoluminescence intensity) is intimately tied to the maximum measured QY (determined from the maximum single-bin photoluminescence intensity).

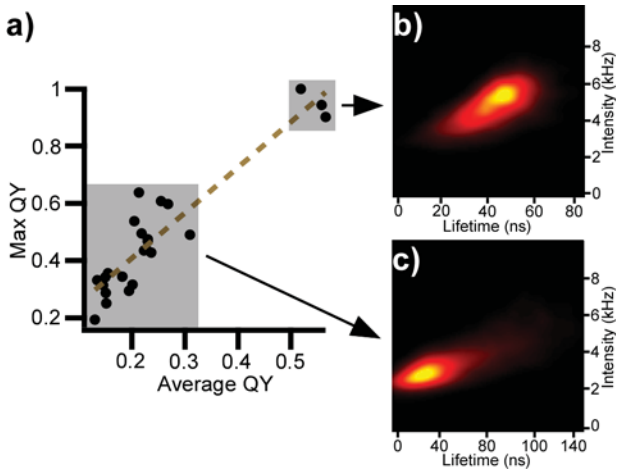

Figure 3: **Quantum yield "pinning" in nonblinking QDs.** (a) Single g-nQDs are "pinned" to characteristic QYs, with single particles expressing a time-invariant single QD QY over the entire PL collection period. Max QY is calculated from the highest-intensity single time bin, while Average QY is calculated from the average QD intensity over the entire collection time. (b) g-nQDs with high QY have FLIDs with tails moving toward low lifetime and low intensity, (c) g-nQDs with low QY show the opposite trend.

This QY pinning phenomenon indicates that any nonradiative process suppressing the single-QD QY is occurring on a time scale much faster than the 100 millisecond binning time, leading to an apparent QY that shows little temporal variance over the entire acquisition

time (always ≥300 seconds). Additionally, we found that QDs with high single-QD QY have long lifetimes and a FLID with a tail extending toward low PL intensity and short lifetime (Figure 3b). Meanwhile, the g-QDs with low single-QD QY show the opposite trend (Figure 3c).

To assist in determination of the underlying cause for the QY heterogeneity, we performed intensity-discriminate $g^{(2)}$ analysis on a g-QD from each of the high- and low-QY subsets. This analysis allows determination of the $g^{(2)}$ value for different intensity levels of the photoluminescence time trace, and has previously been shown to provide information about the charge state of a QD.[26] The structures and optical analyses of the high- and low-QY g-QDs are shown in Figure 4.

The high-QY g-QD possessed a low overall $g^{(2)}$ value and no intensity-dependent $g^{(2)}$ behavior, indicating that the BXQY/SXQY ratio was constant over all measured intensities (4e and 4g). Meanwhile, the low-QY g-QD showed a high $g^{(2)}$ value, but a marked variation of $g^{(2)}$ with intensity (Figure 4f and 4g). Based upon a previously-established precedent, which showed that charged QDs have a drastic level of $g^{(2)}$ variation with PL intensity but neutral QDs do not,[26] these results implicate single-QD charging as the source of low QY. This is corroborated by the shapes of the g-QD FLIDs (Figure 4c and d)—previous spectroscopic and spectroelectrochemical work has shown that a FLID with a tail rising toward high PL intensity and lifetime is indicative of a charged QD.[12,27] We consistently observed this FLID shape for all but the highest QY g-QDs.

The conventional g-QD charging mechanism involves the Auger ionization of a biexciton, followed by excitation with a photon to form a trion. In the CdSe/CdS system used here, the hole is more strongly confined to the core than the electron,[25] so Auger ionization of the hole is stronger than that of the electron. Therefore, biexciton Auger recombination results in excitation of the hole, which can become localized in trap states on the surface of the g-QD. Upon excitation of the g-QD by the next laser pulse, a negative trion is formed.[12,27] The g-QD remains in this charged state, which possesses a characteristically low PL emission

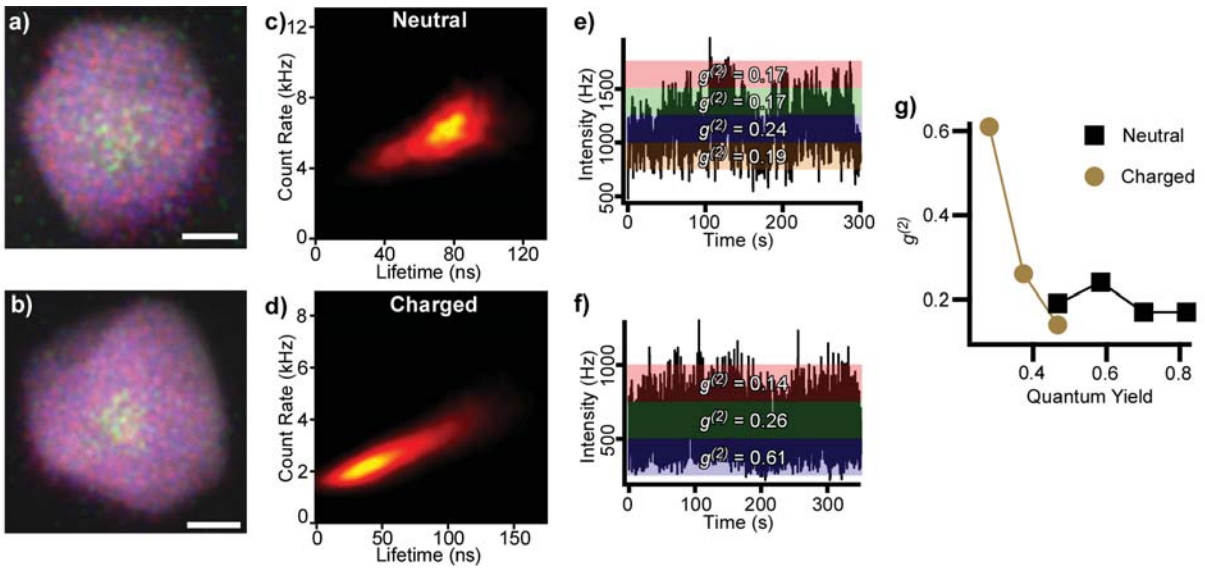

Figure 4: **Further analysis of the influence of charging on single-QD quantum yield.** Shown are corresponding structure / EDS map overlays (a),(b) and optical data (c)-(g) for a representative neutral (a) and charged (b) g-QD. The FLIDs indicate that the g-QDs with highest single-QD QY are neutral, while the g-QDs with heterogeneously distributed lower single-QD QYs are charged. This is confirmed by determining intensity-dependent $g^{(2)}$ values from the photoluminescence intensity transients (e) and (f) of the two g-QDs. For plots (e) and (f), if the photoluminescence intensity of a given time bin falls within the shaded area, the photon arrival events corresponding to that bin are included in the $g^{(2)}$ measurement. This allows us to measure the value of the second-order correlation parameter $g^{(2)}$ for different intensity levels within the overall photoluminescence intensity transient. The $g^{(2)}$ values of each intensity level are indicated on the corresponding shaded areas in (e) and (f), and are also plotted *vs* quantum yield of the corresponding intensity levels in (g). The $g^{(2)}$ values of the neutral g-QD are constant with intensity, while the charged g-QD $g^{(2)}$ values decrease with increasing intensity (g). Scale bars are 5 nm.

intensity due to competition between the radiative and nonradiative trion decay rates, until the hole recombines with the extra electron in the core. In this explanation of QD charging, the density of surface trap states determines the likelihood of charge trapping, and the depth of the respective trap state determines the amount of time the g-QD spends in the corresponding charged state. This would result in QD surface charging that would compete with excitonic recombination and reduce the overall PLQY on the single-QD level. These effects (trap density and depth) combine to dictate the overall percentage of time the g-QD spends in a charged state. This simple mechanism is illustrated in Figure 5.

As a result of the fast time scale of QD charging,[28] the measured QY for each g-QD is

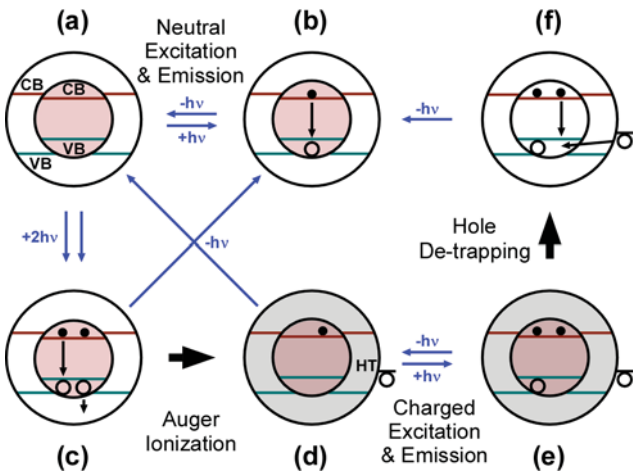

Figure 5: **Mechanism to describe QY heterogeneity.** (a) A single g-QD with quasi-type-II band structure. The valence band is shown as a green line, while the conduction band is indicated with a red line. When the g-QD is struck by a laser pulse, the most common outcome is a single exciton (b) that can recombine radiatively—a process that occurs with near-unity QY. Occasionally, a biexciton is formed (c); Auger ionization of the biexciton results in a negatively-charged g-QD with the hole localized in a hole trap (HT) on the heterostructure surface. After excitation, emission of this singly charged g-QD (e) occurs much less efficiently than photon emission from a neutral g-QD, reducing overall PLQY. The g-QD remains in the charged state until the hole escapes from the hole trap and recombines with the extra electron {(f)→(b) or (d)→(a)}.

temporally invariable and directly related to the rates of charging and discharging for that specific g-QD. For CdSe/CdS heterostructures, charging by a lone charge carrier has been shown to result in quenching of emission intensity and reduction in fluorescence lifetime.[12,29] Therefore, the observed heterogeneity in the low single-QD QY g-QDs is hypothesized to be due to dissimilarity in the charging / discharging rates from QD to QD. This dissimilarity likely arises from the location as well as the nature of the trap sites on the QD.

This charging hypothesis also helps to explain the aforementioned distribution of QYs shown in Figure 2a. The three highest QYs belong to QDs in a neutral state; these QDs emit single excitons from an uncharged state. The rest of the QDs rapidly fluctuate between a charged and neutral state. This is the reason for the large gap between the highest QY "charged" QD and the lowest QY "neutral" QD—only three QDs show ideal emission, while the rest exhibit charging over the length of the measuring period. Because the three QDs with FLIDs indicating neutral emission display similar (high) QYs, we reason that this high

QY state corresponds to ∼100% QY. We base this assumption on previous measurements of near-unity QY "bright" states in binary blinking QDs[30] and similar findings for the brightest states of CdSe/CdS core/thick-shell heterostructure emission.[31,32]

To further confirm our charging hypothesis, we developed a two-state model to explain the relationship between charging and single-QD QY. In our model, the QD is fluctuating between a neutral state with 100% QY and a charged state with QY defined by the minimum measured single-QD QY. Under these assumptions, the relationship between single-QD average QY and single QD average lifetime becomes:

$$Q_{avg} = \frac{\tau_{avg}(Q_{max} - Q_{min}) + \tau_X(\frac{Q_{min}}{2})(2 - Q_{max})}{\tau_X(1 - \frac{Q_{min}}{2})} \quad (1)$$

where Q_{max} and Q_{min} are the single-QD QYs of the neutral and charged states, respectively, τ_X is the neutral exciton lifetime, and τ_{avg} is the average lifetime of the single QD (see Supporting Information for full derivation). For each individual g-QD, we calculated the average QY and average lifetime over the entire measurement period. We then plotted these values to yield Figure 6, which demonstrates the relationship between single-QD QY and τ_{avg}. Each data point shown in Figure 6 represents a single g-QD measured in this study.

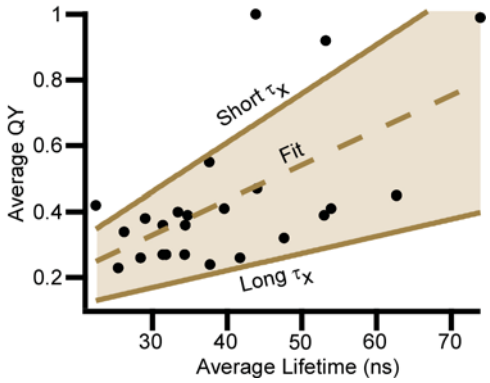

Figure 6: **Modeling the relationship between quantum dot quantum yield and lifetime.** Plotting average quantum yield *vs* average lifetime for each quantum dot reveals a linear relationship between the parameters. This linear model assumes that a single QD is in either a neutral or singly charged state. Because the neutral exciton lifetime varies between dots, an upper and lower bound corresponding to short and long neutral exciton lifetime are plotted.

The derived model is shown for a range of τ_X varying from 66 to 189 ns, corresponding to the minimum and maximum measured τ_X values for the investigated sample. One of the factors that causes a variation in neutral exciton lifetime is the orientation of the QD. There is a small, but non-negligible, dependence of QD emission on the orientation of individual g-QDs (see Supporting Information). This variation in orientation is manifested in a concomitant variation in neutral exciton lifetime of single g-QDs. For this reason, we see that it is helpful to consider QD orientation when fitting our data. The agreement between our single-charging model and the measured data confirms that such a model is sufficient to describe the observed variations in single-QD QY.

In previous work, we have shown that the presence of crystalline defects at the core/shell interface results in reduction of the PL "on" time of individual QDs. This phenomenon likely occurs due to the presence of surface defects that form as a result of the stacking faults found at the core/shell interface.[10] In the system studied here, this type of surface defect would occur as a result of continuation of stacking faults at the core/shell interface outward to the surface, and would be expressed as a grain boundary in the thick CdS shell of the g-QD heterostructure. However, stacking faults at the core/shell interface would be difficult to observe in our HAADF images because this interface is typically obscured by the large particle volume, which lowers the chance of the nanocrystal being aligned perfectly on a zone-axis—a requirement for high resolution imaging.

In addition to the above mentioned defects, several other sources of surface defects are known which could contribute to g-QD charging, and consequently reduce the g-QD PLQY. Ligand coverage is especially important, and steric crowding at the surface of the nanocrystal can prevent complete ligand passivation of the surface.[33] Further, under-coordinated atoms at the surface can act as trap states that could localize charge carriers. Previous results have also shown that surface dynamics of the nanocrystal and passivating ligands can result in surface trapping;[34,35] this type of defect has been used to describe reduced PL emission as well as QD blinking behavior.[36,37] Although g-QDs benefit from a thick inorganic shell, the

exciton recombination dynamics are not entirely divorced from the QD surface due to the large energy of Auger ionization; minimization of defects related to ligand coverage is key in increasing the overall PLQY by reducing g-QD charging.

Finally, with regard to $g^{(2)}$ measurements—as has been noted previously, the $g^{(2)}$ value, which can be calculated as the center peak-to-side peak ratio for the second order intensity correlation histogram, is known to be equal to the biexciton quantum yield divided by the single exciton quantum yield (BXQY/SXQY).[7,23] Therefore, the actual BXQY value is different than the $g^{(2)}$ value for the QDs studied. In the case of the g-QDs studied here, because the value of the SXQY is typically lower than 100%, the deviation of $g^{(2)}$ from BXQY is significant. When the experimentally measured single-QD QY is used to calculate BXQY according to this relationship, the average BXQY value for the observed QDs is reduced by a factor of ∼2 from the measured $g^{(2)}$ value, as shown in Figure 7.

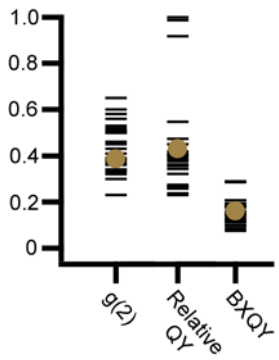

Figure 7: **The use of single-QD quantum yield to determine BXQY.** The $g^{(2)}$ values measured for each QD are used, in conjunction with the measured single g-QD QY, to calculate BXQY for each QD. The tight grouping of BXQY values indicates that charging, and not BXQY variation, is the main source of $g^{(2)}$ heterogeneity.

While $g^{(2)}$ values show a wide, heterogeneous distribution, BXQY values calculated using measured QY show a very narrow distribution, suggesting that Auger suppression is quite uniform across the sample (radiative recombination from the biexciton state is similar for all g-QDs). This also indicates that observed variations in $g^{(2)}$ are mainly a result of variation in the degree of charging in individual g-QDs, and the inherent BXQY for each g-QD is fairly constant.

Conclusion

Reduced PLQY is intimately linked with surface defects—and remarkably, these fine defects seem to have little to do with overall morphology of the g-QDs. Rather, such defects likely result from synthetically controllable conditions such as ligand selection, ligand ratios, shelling temperature, and the level of alloying at the core/shell interface.[38] This would explain the recent success of, for example, high-temperature shelling procedures[39] and graded alloy syntheses[40] in obtaining high-QY QD samples.

A tandem of HAADF-STEM and PL spectroscopy has proven crucial for a comprehensive understanding of single QD photoluminescence behavior. Without this pairing, it would not have been possible to determine single-QD QY or to identify single-QD QY heterogeneity among individual nonblinking QDs. Further analysis of single-photon emission events was necessary to elucidate the mechanism by which single-QD QY is reduced—namely single-QD charging. Also, in light of the recent new understanding pertaining to the origin of non-blinking emission in some QD samples,[41] our approach affords a novel means for straightforward, unambiguous confirmation that steady emission signals are correlated with a QD emitter.

Our data indicate that, even within nonblinking QDs, quantum yield heterogeneity arises from charging processes that occur on a time scale much faster than is measurable using conventional single-QD photoluminescence spectroscopy. We show that such quantum yield heterogeneity, along with the noted lack of a "dark" fraction of QDs, can account for g-QD ensembles simultaneously characterized by moderate quantum yields yet also nearly fully nonblinking behavior. This observation is supported by a recent report of long-lived charged states measured in ensemble solutions of CdSe QDs.[42] We also note that QY pinning is due to rapid charging and discharging from a singly-charged state, rather than multiple discrete charged states for individual nanocrystals—an assertion that is supported by previous research on the quasi-type-II band gap offset between CdSe and CdS,[25] and also by our own model.

The developed method of precise determination of relative QY based on the *measured* rather than *presumed* volume of single QDs—for which the size distribution is heterogeneous—is important in advancing the understanding of single QD photophysics. Our comprehensive description of single g-QDs was instrumental in uncovering relative QY heterogeneity, the lack of a "dark" fraction of g-QDs, pinning of single g-QDs to specific QYs, and an unexpectedly homogeneous distribution of BXQYs.

Experimental

Determination of Single Quantum Dot Quantum Yield

The absorption cross section is calculated according to the following modified equation:[8,43]

$$\alpha = V\alpha_w|f_w|^2\frac{n_w}{n_{medium}} \tag{2}$$

where σ is the absorption cross-section of the g-QD heterostructure, α_w is the absorption coefficient, $|fw|^2$ is a correction factor, n_w is the refractive index of CdS, n_{medium} is the refractive index of air, and V is the rough volume of the heterostructure measured from the HAADF intensity. We approximate the value of the QD volume by setting the maximum measured HAADF density to the value of the maximum measurable two-dimensional diameter (the Feret diameter, R_F) and calculating *via* the equation:

$$V_{QD} = A\sum\left\{\frac{\phi_i}{\phi_{max}}\gamma R_F\right\} \tag{3}$$

where A is the two-dimensional projection of the area of the QD on the TEM support film in nm^2, ϕ_i is the integrated density per pixel, and γ is the number of pixels per nm^2. The absorption cross-section can then be used to calculate the relative QY for any given intensity using the simple relationship:

$$QY \propto \frac{I}{\sigma} \tag{4}$$

where I is the measured photoluminescence intensity. This allows us to determine the QY ratio of all g-QDs and normalize to the highest QY in the studied population.

For calculation of QD volume, detection of scattered electrons was presumed to scale linearly with material thickness as demonstrated previously.[44,45] Also, the approximation is made that QD height does not vary drastically from the width measured from 2D cross-sections. Additionally, in contrast to smaller core/shell QDs, the CdSe core here accounts for <5% of the total heterostructure volume. Because the intensity contrast of the HAADF varies nonlinearly as a function of atomic number Z ($I \propto Z^{\alpha}$), where the variable α is always <2,[44] any overestimation in the QD volume due to atomic number contrast difference between CdSe and CdS would be <2% and within the error of the instrument. Therefore, a correction factor for variable atomic number contrast was deemed unnecessary.

Nanocrystal Synthesis

Materials. Selenium (1-3 mm shot, 99.999%), CdO powder (99.998%), and oleic acid (OLAC, 90%) were purchased from Alfa Aesar. Sulfur (99.999%), oleylamine (OLAM, C18 content 80-90%), 1-octadecene (ODE, 90%), and octadecane (OD, 90%) were purchased from Acros Organics. Trioctylphosphine (TOP, 90%) was purchased from Sigma Aldrich, and trioctylphosphine oxide (TOPO, 90%) was purchased from Strem Chemicals. All chemicals were used as received without further purification, and all syntheses were performed under Ar atmosphere using standard air-free Schlenk techniques.

Preparation of Stock Solutions. 0.5 M Cd(II)oleate solution was prepared by dissolving CdO in OLAC at 180 °C, followed by removal of water under vacuum at 80 °C. Similarly, 0.2 M Cd(II)oleate solutions (10:1 mol/mol OLAC:Cd^{2+}) were prepared by dissolving CdO in a mixture of OLAC and either OD or ODE. 0.2 M sulfur solutions were prepared by dissolving

sulfur powder in either OD or ODE at 180 °C. Stock solutions of trioctylphosphine-selenium complex (TOP-Se) were typically 1M, and prepared by stirring Se in TOP overnight under air-free conditions.

Synthesis of CdSe quantum dot (QD) cores. CdSe QD cores were prepared according to previously published literature, with slight modifications.[18,46] Briefly, a room-temperature solution containing 4 mL of 1 M TOP-Se, 3 mL OLAM, and 1 mL ODE was rapidly injected into a 300 °C solution containing 0.750 mL of 0.5 M Cd(II)oleate, 1.2 g TOPO, and 9 mL of ODE. The temperature recovered and was maintained at 270 °C, and after 5 min, a solution containing 3 mL of 0.2 M Cd(II)oleate in ODE and 6 mL of 1 M TOP-Se was added dropwise over ∼1h. The resulting nanocrystals exhibited a lowest energy absorbance peak at 605 nm, corresponding to an approximate size of 4.8 nm.[47]

CdSe/CdS "giant" quantum dot (gQD) synthesis: CdSe/CdS gQDs were synthesized using a SILAR approach, following previously published methods.[18] Briefly, 2.0×10^{-7} mol of purified CdSe cores, dispersed in hexanes, were added to a mixture of 5 mL OLAM and 5 mL OD. Hexanes were removed in vacuo at 80 °C, and the temperature was raised to 240 °C for SILAR. Alternating injections of 0.2 M Cd(II)oleate and 0.2 M sulfur (both in OD) were performed in a dropwise fashion, allowing 3 h of solution-phase annealing after each Cd(II)oleate addition and 1 h after each S addition. The delivered precursor volumes were calculated34 to yield one ML of CdS shell per addition cycle, for a total of 16 ML CdS.

Sample Preparation

A transmission electron microscopy (TEM) support film coated with polystyrene latex sphere markers was prepared for correlation as reported previously.[10] The synthesized g-QD samples were diluted to ∼1 nM concentration in hexanes. Approximately 10 μL of this solution was then dropcasted onto the prepared support film (Ted Pella, PELCO 8 nm Ultra-Flat Silicon Dioxide Support Film) and the residual hexanes solution was immediately wicked away with a KimWipe.

Single QD Spectroscopy

After preparation, the support film was placed, face-down, on a No. 1 glass cover slip. The sample was then imaged by raster scanning with a 405 nm pulsed excitation source (PicoQuant PDL; 30 ps pulse width, 2.5-10 MHz repetition rate). This setup has previously been described in full detail.[27] The repetition rate was chosen to ensure that the PL lifetime trace decayed fully before the arrival of subsequent pulses. Excitation and collection of emission occurred through an oil-immersion Olympus objective with N.A. of 1.3. The emitted photons were collected onto two avalanche photodiodes (APDs; SPCM-AQRH-14, Perkin Elmer) in a Hanbury-Brown Twiss interferometric configuration. We verified that, for all QDs studied, the number of excitations per pulse $<N>$ was less than 0.2. This was done according to a previously established method of measuring $<N>$ as a function of excitation intensity.[27]

Homebuilt software was used to perform all analysis of photoluminescence data and generate FLIDs.

Electron Microscopy

After all relevant photoluminescence data had been collected, support films were stored in a grid holder until electron microscopy could be performed. Scanning transmission electron microscopy images were obtained using a Tecnai Osiris operating at 200 kV, with a spot size set to 10 (to reduce charging effects) and a camera length of 220 mm for HAADF imaging. HAADF-STEM imaging was chosen over HRTEM imaging since the white-on-dark-contrast for STEM greatly facilitates the location of individual quantum dots at low magnifications. Patterns of polystyrene were used to align the STEM image and distances measured from the optical microscope were used to identify regions of interest. Large area STEM images were used to identify neighboring particles and possible dark particles. After obtaining a high resolution STEM image of a particle, the spot size was lowered to 4 yielding $\sim$1.5 nA of beam current with a probe size on the order of 0.5 nm. These conditions, in conjunction

with a highly efficient Super-X^{TM} EDS detection system, enabled rapid collection of EDS spectrum maps with a minimal number of scans (∼30 seconds total acquisition time). EDS hypermaps were collected using Bruker's Esprit software.

Acknowledgement

This work was supported in part by the National Science Foundation CHE grant 1213758 and National Science Foundation EPS 1004083 (TN-SCORE). JAH, HH and FW acknowledge primary support by a Division of Materials Science and Engineering DOE, OBES grant (2009LANL1096) for g-QD development guided by defining structure-function relationships. Work performed in part at the Center for Integrated Nanotechnologies, a U.S. Department of Energy (DOE), Office of Basic Energy Sciences (OBES) Nanoscale Science Research Center & User Facility as part of User Project U2014B0001.

Supporting Information Available

Additional discussion and commentary regarding the calculation of volume of single g-QDs, and full representation of structural, chemical, and optical analysis of all g-QDs studied here.

This material is available free of charge via the Internet at `http://pubs.acs.org/`.

References

(1) Dickson, R. M. *J. Phys. Chem. Lett.* **2011**, *2*, 2044–2045.

(2) Castelli, A.; Meinardi, F.; Pasini, M.; Galeotti, F.; Pinchetti, V.; Lorenzon, M.; Manna, L.; Giovanella, U.; Moreels, I.; Brovelli, S. *Nano Lett.* **2015**, *15*, 5455–5464.

(3) Kim, T. H.; Cho, K. S.; Lee, E. K.; Lee, S. J.; Chae, J.; Kim, J. W.; Kim, D. H.;

Kwon, J. Y.; Amaratunga, G.; Lee, S. Y.; Choi, B. L.; Kuk, Y.; Kim, J. M.; Kim, K. *Nat. Photon.* **2011**, *5*, 176–182.

(4) Foucher, C.; Guilhabert, B.; Laurand, N.; Dawson, M. D. *Appl. Phys. Lett.* **2014**, *104*, 141108.

(5) Bao, J.; Bawendi, M. G. *Nature* **2015**, *523*, 67–70.

(6) Michler, P.; Imamoglu, A.; Mason, M. D.; Carson, P. J.; Strouse, G. F.; Buratto, S. K. *Nature* **2000**, *406*, 968–970.

(7) Nair, G.; Zhao, J.; Bawendi, M. G. *Nano Lett.* **2011**, *11*, 1136–1140.

(8) Park, Y. S.; Malko, A. V.; Vela, J.; Chen, Y.; Ghosh, Y.; Garcia-Santamaria, F.; Hollingsworth, J. A.; Klimov, V. I.; Htoon, H. *Phys. Rev. Lett.* **2011**, *106*, 187401.

(9) Rosenthal, S. J.; Chang, J. C.; Kovtun, O.; McBride, J. R.; Tomlinson, I. D. *Chem Biol.* **2011**, *18*, 10–24.

(10) Orfield, N. J.; McBride, J. R.; Keene, J. D.; Davis, L. M.; Rosenthal, S. J. *ACS Nano* **2015**, *9*, 831–839.

(11) Mangel, S.; Aronovitch, E.; Enyashin, A. N.; Houben, L.; Bar-Sadan, M. *J. Am. Chem. Soc.* **2014**, *136*, 12564–12567.

(12) Galland, C.; Ghosh, Y.; Steinbruck, A.; Sykora, M.; Hollingsworth, J. A.; Klimov, V. I.; Htoon, H. *Nature* **2011**, *479*, 203–207.

(13) Qin, W.; Guyot-Sionnest, P. *ACS Nano* **2012**, *6*, 9125–9132.

(14) Ebenstein, Y.; Mokari, T.; Banin, U. *Appl. Phys. Lett.* **2002**, *80*, 4033–4035.

(15) Koberling, F.; Mews, A.; Philipp, G.; Kolb, U.; Potapova, I.; Burghard, M.; Basche, T. *Appl. Phys. Lett.* **2002**, *81*, 1116–1118.

(16) Koberling, F.; Kolb, U.; Philipp, G.; Potapova, I.; Basche, T.; Mews, A. *J. Phys. Chem. B* **2003**, *107*, 7463–7471.

(17) Chen, Y.; Vela, J.; Htoon, H.; Casson, J. L.; Werder, D. J.; Bussian, D. A.; Klimov, V. I.; Hollingsworth, J. A. *J. Am. Chem. Soc.* **2008**, *130*, 5026–5027.

(18) Ghosh, Y.; Mangum, B. D.; Casson, J. L.; Williams, D. J.; Htoon, H.; Hollingsworth, J. A. *J. Am. Chem. Soc.* **2012**, *134*, 9634–9643.

(19) Mahler, B.; Spinicelli, P.; Buil, S.; Quelin, X.; Hermier, J. P.; Dubertret, B. *Nat. Mater.* **2008**, *7*, 659–664.

(20) Garcia-Santamaria, F.; Chen, Y. F.; Vela, J.; Schaller, R. D.; Hollingsworth, J. A.; Klimov, V. I. *Nano Lett.* **2009**, *9*, 3482–3488.

(21) Vela, J.; Htoon, H.; Chen, Y. F.; Park, Y. S.; Ghosh, Y.; Goodwin, P. M.; Werner, J. H.; Wells, N. P.; Casson, J. L.; Hollingsworth, J. A. *J. Biophotonics* **2010**, *3*, 706–717.

(22) McBride, J. R.; Kippeny, T. C.; Pennycook, S. J.; Rosenthal, S. J. *Nano Lett.* **2004**, *4*, 1279–1283.

(23) Zhao, J.; Chen, O.; Strasfeld, D. B.; Bawendi, M. G. *Nano Lett.* **2012**, *12*, 4477–4483.

(24) Pons, T.; Medintz, I. L.; Farrell, D.; Wang, X.; Grimes, A. F.; English, D. S.; Berti, L.; Mattoussi, H. *Small* **2011**, *7*, 2101–2108.

(25) Keene, J. D.; McBride, J. R.; Orfield, N. J.; Rosenthal, S. J. *ACS Nano* **2014**, *8*, 10665–10673.

(26) Paulite, M.; Acharya, K. P.; Nguyen, H. M.; Hollingsworth, J. A.; Htoon, H. *J. Phys. Chem. Lett.* **2015**, *6*, 706–711.

(27) Galland, C.; Ghosh, Y.; Steinbruck, A.; Hollingsworth, J. A.; Htoon, H.; Klimov, V. I. *Nat. Commun.* **2012**, *3*.

(28) Underwood, D. F.; Kippeny, T.; Rosenthal, S. J. *J. Phys. Chem. B* **2001**, *105*, 436–443.

(29) Jha, P. P.; Guyot-Sionnest, P. *ACS Nano* **2009**, *3*, 1011–1015.

(30) Brokmann, X.; Coolen, L.; Dahan, M.; Hermier, J. P. *Phys. Rev. Lett.* **2004**, *93*, 107403.

(31) Javaux, C.; Mahler, B.; Dubertret, B.; Shabaev, A.; Rodina, A. V.; Efros, A. L.; Yakovlev, D. R.; Liu, F.; Mayer, B.; Camps, G.; Biadala, L.; Buil, S.; Quelin, X.; Hermier, J. P. *Nat. Nanotech.* **2013**, *8*, 206–212.

(32) Nasilowski, M.; Spinicelli, P.; Patriarche, G.; Dubertret, B. *Nano Lett.* **2015**, *15*, 3953–3958.

(33) Ip, A. H. et al. *Nat. Nanotech.* **2012**, *7*, 577–582.

(34) McBride, J. R.; Pennycook, T. J.; Pennycook, S. J.; Rosenthal, S. J. *ACS Nano* **2013**, *7*, 8358–8365.

(35) Pennycook, T. J.; McBride, J. R.; Rosenthal, S. J.; Pennycook, S. J.; Pantelides, S. T. *Nano Lett.* **2012**, *12*, 3038–3042.

(36) Voznyy, O.; Sargent, E. H. *Phys. Rev. Lett.* **2014**, *112*, 157401.

(37) Voznyy, O.; Thon, S. M.; Ip, A. H.; Sargent, E. H. *J. Phys. Chem. Lett.* **2013**, *4*, 987–992.

(38) Busby, E.; Anderson, N. C.; Owen, J. S.; Sfeir, M. Y. *J. Phys. Chem. C* **2015**, DOI: 10.1021/acs.jpcc.5b08243.

(39) Chen, O.; Zhao, J.; Chauhan, V. P.; Cui, J.; Wong, C.; Harris, D. K.; Wei, H.; Han, H. S.; Fukumura, D.; Jain, R. K.; Bawendi, M. G. *Nat. Mater.* **2013**, *12*, 445–451.

(40) Harrison, M. A.; Ng, A.; Hmelo, A. B.; Rosenthal, S. J. *Isr. J. Chem.* **2012**, *52*, 1063–1072.

(41) Rabouw, F. T.; Cogan, N. M. B.; Berends, A. C.; van der Stam, W.; Vanmaekelbergh, D.; Koenderink, A. F.; Krauss, T. D.; Donegá, C. M. Non-blinking single-photon emitters in silica. http://arxiv.org/abs/1509.07262, 2015.

(42) Rabouw, F. T.; Kamp, M.; van Dijk-Moes, R. J. A.; Gamelin, D.; Koenderink, A. F.; Meijerink, A.; Vanmaekelbergh, D. *Nano Lett.* **2015**, *15*, 7718–7725.

(43) Leatherdale, C. A.; Woo, W. K.; Mikulec, F. V.; Bawendi, M. G. *J. Phys. Chem. B* **2002**, *106*, 7619–7622.

(44) Wang, Z. W.; Li, Z. Y.; Park, S. J.; Abdela, A.; Tang, D.; Palmer, R. E. *Phys. Rev. B* **2011**, *84*, 073408.

(45) LeBeau, J. M.; Findlay, S. D.; Allen, L. J.; Stemmer, S. *Phys. Rev. Lett* **2008**, *100*, 206101.

(46) Mahler, B.; Lequeux, N.; Dubertret, B. *J. Am. Chem. Soc.* **2010**, *132*, 953–959.

(47) Yu, W. W.; Qu, L. H.; Guo, W. Z.; Peng, X. G. *Chem. Mater.* **2003**, *15*, 2854–2860.

Graphical TOC Entry